Impact of embedded Co nanoparticles on local magnetic properties of L10-FePt films

Charles Paléo, Fabrice Wilhelm, Philippe Ohresser, Edwige Otero, André Dias, Nora Dempsey, Véronique Dupuis, Damien Le Roy

Impact of embedded Co nanoparticles on local magnetic properties of $L1_0$-FePt films

Charles Paléo[1], Fabrice Wilhelm[2], Philippe Ohresser[3], Edwige Otero[3], André Dias[4], Nora M. Dempsey[4], Véronique Dupuis[1], and Damien Le Roy[1]

[1] Univ Lyon, Univ Claude Bernard Lyon 1, CNRS, Institut Lumière Matière, F-69622, Villeurbanne, France
[2]The European Synchrotron Radiation Facility (ESRF), 38000 Grenoble, France
[3] Synchrotron SOLEIL, L'Orme des Merisiers, 91190 Saint-Aubin, France
[4]Université Grenoble Alpes, CNRS, Grenoble INP, Institut Néel, 38000 Grenoble, France

Hard-magnetic films with precisely tuned switching fields are of great interest for advanced magnetic microsystems. Here we report on the specific evolution of semi-hard magnetic properties of $L1_0$-FePt films integrating a graded concentration of soft cobalt nanomagnets. These nanocomposites are prepared by the combination of MS-LECBD and e-beam evaporation techniques where 8 nm Co nanoparticles are embedded with various x atomic concentration up to 50%, into Fe/Pt multilayers. A subsequent annealing allows us to reach the alloy chemical order for the FePt matrix by conserving Co-rich nanometer-sized inclusions. The focus is put on the interplay between the local microstructure and the coercive magnetic field through a combinatorial approach that involves local determinations of composition, magnetization reversal from scanning magneto-optical Kerr effect and element-specific spin and orbital magnetic moments from X-ray magnetic circular dichroism performed at the Co and Fe L-edges of absorption. We show how the nanostructuration changes the magnetic coercivity, and how both Co and Fe effective magnetic spin moments evolve with the composition of the nanocomposite film.

***Index Terms*—Semi-hard magnet, Nanocomposite, Nanoparticles.**

I. Introduction

Among all magnetically-hard materials, the chemically ordered $L1_0$-FePt compound favorably combines high magnetocrystalline anisotropy, a large magnetization, a relatively high thermal stability (Curie temperature of 750 K), and a high resistance against corrosion **[1]**. Therefore, despite its high cost, $L1_0$-FePt is a material of choice to implement hard magnetic structures in micrometer-sized devices **[2]**. There is a rich literature showing how to tailor some of its hard magnetic properties, like the uniaxial anisotropy **[3-5]** and the magnetization switching field **[5]**, while conforming to the constraints of microfabrication and facilitating its implementation in devices. Increase the magnetization with magnetically soft nano-inclusions is one more way to tune the magnetic properties of $L1_0$-FePt semi-hard films. In addition, a controlled nanostructuration of these films could give interesting insights for building soft-in-hard nanocomposite permanent magnets.

In this work, we produce FePt films integrating face-centered-cubic (fcc) Co nanoparticles (Co-NPs), using a mass selected cluster beam deposition (MS-LECBD) technique, combined with an electron beam evaporator **[6]**. After annealing under ultra-high vacuum (UHV) conditions, the films present a gradient of Co-NPs inclusions into a $L1_0$-FePt matrix. This compositionally graded film can serve to screen the evolution of magnetic properties as a function of the concentration using local characterization techniques. Within the combinatorial approach **[7,8]**, several magnetic scanning probe techniques have been developed for high throughput studies, including superconducting quantum interference device (SQUID)-based microscopy **[9,10]** or Hall microscopy **[11,12]**. Here we use a scanning magneto-optical Kerr effect (MOKE) system with a microsecond pulsed magnetic field source that produces fields up to 10 T **[13]**. In particular, we study the evolution of the coercive magnetic field with the volume fraction of Co-NPs. In parallel, we determine the specific atomic magnetic moments from X-ray magnetic circular dichroism (XMCD), as a function of the concentration of the soft inclusions. To unveal the impact of the nanostructuration, we compare the results with the ones obtained on Co-Fe-Pt alloyed films of similar thicknesses replacing Co-NPs by Co atomic layers **[6]**.

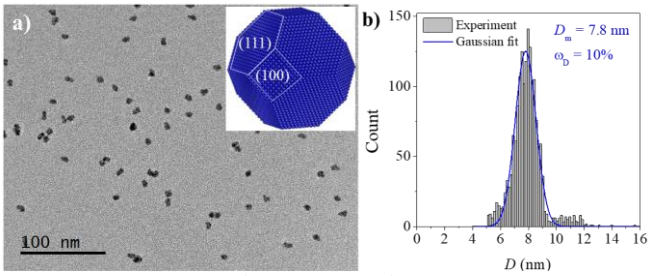

Fig. 1. (a) TEM image of an assembly of Co NPs. The inset shows a schematic view of a fcc-Co truncated octahedron of around 7.9 nm in size. (b) Statistical analysis of the Co NPs' diameter *D*, from TEM analysis.

II. Experimental Methods

A. Preparation of the $L1_0$-FePt films integrating Co-NPs

Co-NPs are produced by gas-phase condensation, in a MS-LECBD system using laser vaporization, and are deposited in a soft-landing regime **[14]**. Our experimental set-up is also equipped with an electron beam evaporator with four crucibles for atomic deposition of a matrix. This equipment permits to embed the NPs in any hosting material, by alternately

depositing NPs and atomic layers. In this study, the deposition incident angles on the substrate are of 45°, both for the cluster beam and for the atoms from the evaporator. **Fig.1a** shows a transmission electron microscopy (TEM) image of the Co-NPs supported on an amorphous carbon membrane. The **Fig.1b** displays the resulting size distribution. In this work, Co-NPs are selected in mass, leading to a Gaussian distribution of diameter centered at 7.9 nm with a 15% dispersion. In our previous work, we showed that such as-produced Co-NPs crystallize in a fcc structure, and form truncated octahedra exhibiting the co-existence of (111) and (100) facets **[15]**, as expected from the Wulff construction model and represented in the inset of **Fig. 1a**.

B. Mapping of the Co-NPs areal density

The same MS-LECBD settings were used for all Co-NP depositions. We prepared specific samples to calibrate the Co-NPs deposition profile by means of atomic force microscopy (AFM). Co-NPs were deposited onto on a silicon substrate with a native SiO_2 layer. Prior to deposition, Au/Ti marks for *X* and *Y* coordinates along two orthogonal directions of the plane were patterned by photolithography and lift-off techniques. AFM images over areas of 1 μm^2 were then recorded at every millimeter along the *X* and *Y* directions. **Fig.2a** shows the reconstructed map of the NPs' density *n* (number of NPs per μm^2). This same study was conducted once again at several weeks interval, confirming that the calibration did not change over the time of this study. Note that the calibration was further validated by superimposing the Co X-rays Absorption Spectroscopy (XAS) signal mapping prior to Extended X-Ray Absorption Fine Structure (EXAFS) and XMCD local measurements.

The $Co_x@(FePt)_{100-x}$ films are deposited at room temperature in a UHV chamber (base pressure of 10^{-10} mbar), on a silicon substrate with a native SiO_2 layer. The nanocomposite structure is obtained by sequential deposition of Co-NPs, and atomic bilayers of Fe (1.2 nm in thickness) and Pt (1.4 nm in thickness), repeated six times in total. The total deposited thickness of Fe-Pt is of 15.6 nm. The film is subsequently annealed under vacuum at 700°C for 20 min in order to obtain the $L1_0$-FePt hard magnetic phase **[6,16]**, evidenced by the appearance of the (001) superstructure peak in the specular X-ray diffraction pattern. Throughout the deposition area, the surface coverage of the Co-NPs in each layer is of about 21%, as estimated from a Faraday cage placed in deposition chamber. Due to the incidence angle of 45°, the deposition areas of both the NPs' beam and the atomic flux from the evaporator form ellipses, with a long axis to short axis ratio of √2. The atomic flux from the evaporator covers a larger area of the substrate than the NPs beam, characterized by a long axis of 20 mm and 8 mm, respectively.

III. Results and Analysis

A. Compositionally-graded Co@FePt NP films

The Co-NPs' deposition footprint forms an ellipse with a long axis to short axis ratio of 1.35, slightly less than √2 (**Fig.2a**). The density of deposited Co-NPs is nearly symmetric with respect to the major axis of the ellipse, but highly asymmetric along the *Y* direction.

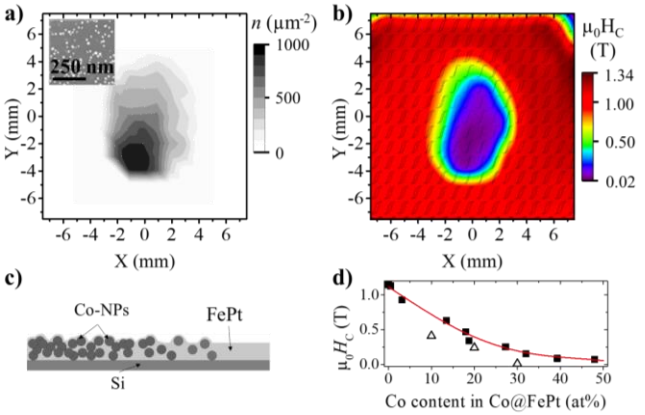

Fig. 2. (a) Reconstructed map of the Co-NPs' density on a surface, from AFM observations (as illustrated by the image of the inset). The color scale represents the number of NPs per μm^2; denoted as *n*. For this, images of area of 1×1 μm^2 were recorded. (b) Coercive field mapping over the NPs' deposition area of the $Co_x@FePt_{100-x}$ film, from scanning MOKE with measured hysteresis cycles superimposed. (c) Schematic profile of the compositionally-graded $Co_x@FePt_{100-x}$ film, as deposited. (d) Deduced compositional dependence of H_C (continuous line is a third order polynomial interpolation). The open symbols show the H_C values of our reference Co-Fe-Pt alloyed films.

As a result, along the *Y* axis at $X = 0$, and by moving away from the maximum (at $Y \sim -3$), the density gradient is about six times larger when going downward as compared to in the upward direction. In the upward direction, *n* varies from 1100 NPs/μm^2 down to 0, over 8 mm.

The surface area covered by the Co-NPs is significantly smaller than the one covered by the FePt film. Besides, the thickness and the magnetic properties of the FePt matrix, studied by AFM, X-ray reflectivity and scanning MOKE are found to be even over an area that is 6 times larger than the region containing NPs. Therefore, a single deposition contains a large region of homogeneous Co-free FePt film. It is worth mentioning here that AFM observations of the film's surface reveals a smooth surface with 1 nm roughness. The deposition parameters are set to obtain a compositionally-graded $Co_x@(FePt)_{100-x}$ film with *x* varying from 0 to 50% (atomic proportions), over 8 mm.

B. Magnetic properties of the $Co_x@(FePt)_{100-x}$ films

Local hysteresis loops are measured using a scanning polar MOKE system **[13]**. The system is equipped with a bipolar pulsed current source coupled with a Cu-coil of inner (outer) diameter ca. 3 (10) mm. The length of individual field pulses is of the order of 16 μs, and the delay between positive and negative field pulses is about 10 ms. The hollow center of the coil allows the incident and reflected light beams to pass through. The film under measurement is scanned in plane below the coil using an X-Y stage (minimum step size of 2 μm) and the coil to sample distance is set to 100 μm.

Out-of-plane magnetization curves are measured every 500 μm in the X and Y directions across the film's surface. **Fig.2b** shows the reconstructed map of the coercive field H_C. The

color scale shows the value of H_C, whose variation well matches with the region of the film that contains the Co-NPs. Combining the density of deposited Co-NPs and the H_C values leads to the average continuous curve of **Fig.2d**. The symbols correspond to the variation of H_C at X = 1 and Y varying from 0 to 6 mm.

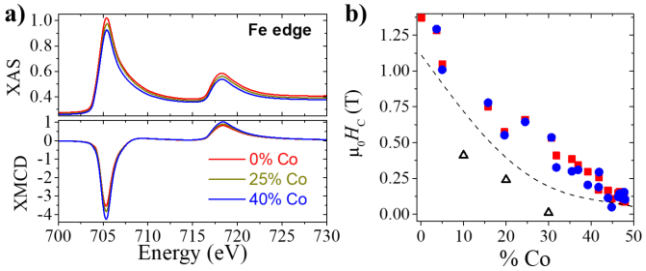

Fig. 3. (a) TEY acquisition of the XAS and XMCD at Fe $L_{2,3}$ edges for x of 0, 25, and 40%. (b) H_C measured at the Fe and Co L_3-edges as a function of the Co content x. The XMCD data recorded on Fe edge (red squares) and on Co edge (blue circle) are compared to the values of H_C of the Co-Fe-Pt alloyed films measured in a SQUID magnetometer (open symbols). The dashed line is the polynomial fit of the MOKE results presented in Fig.2.

Moreover, scanning XMCD measurements have also been carried out (on the DEIMOS beamline at SOLEIL synchrotron **[17]**) in total electron yield (TEY) and fluorescence to probe element-specific magnetic properties at the $L_{2,3}$ edges of Fe and Co. Absorption spectra at both Fe (**Fig.3a**) and Co (not shown) edges reveal clean metallic signals that allow to extract the magnetic moments. The sample are scanned every 500 µm along the long axis of the Co cluster deposition area to analyze the evolution of the atomic magnetic moments with the Co content. The magnetic moment reversal recorded at the L_3 edge of Fe and Co (**Fig.3b**) shows a simultaneous reversal over the whole range of Co-NPs content (0 to 50%), indicating a strong magnetic coupling between soft and hard regions in these graded-interface nanocomposite films. The decay of H_C with the Co content measured by XMCD is less pronounced than the one obtained from the MOKE analysis (shown on Fig.2d and recalled by the dashed line on Fig.3b). This discrepancy might be due to the difference in the probed depth. Indeed, the sensitivity of XMCD TEY measurements is limited to the first 5 nm **[18]**, while it is of around 20 nm in the case of MOKE measurements **[13]**. Therefore, while the entire film's thickness is probed in MOKE, only the top quarter of the film is analyzed in XMCD. However, regardless the employed techniques, the nanocomposite film shows larger H_C values than the reference Co-Fe-Pt alloyed films. XAS spectra were recorded at room temperature, under an external field of 5 T parallel to the incident X-ray beam and perpendicularly to the sample plane (90°). XMCD spectra on Fe $L_{2,3}$ peaks show a systematic increase of intensity when the Co content increases, as expected for higher amount of Co-Fe bonds (**Fig.4a,c**) **[20]**.

C. Co and Fe orbital and effective spin moments

Sum rules **[21,22]** have been applied to quantify the orbital and effective spin moments of Co and Fe on TEY measurements. The spectra are normalized and the continuum is subtracted from the XAS for each polarization. The number of holes used in calculation is 3.7 for Fe (reported value for $L1_0$-FePt **[23]** and 2.174 for Co (FeCo alloy value **[24]**). The magnetic dipole term, which cannot be neglected in highly anisotropic phases such as $L1_0$-FePt **[25]**, is not subtracted. Therefore, only the effective spin moment is being shown and compared to other effective spin moments found in the literature **[23,26-28]** (denoted μ_S(Fe) and μ_S(Co) for Fe and Co, respectively). The results are displayed as a function of the Co content on **Fig.4**, for Fe (**Fig.4a,c**) and Co (**Fig.4b,d**). To our knowledge, only a few works, like Sakamoto *et al*. **[25]**, were reported on the element-specific magnetic moments of the ternary FeCoPt alloy. The effective spin moment at Fe edges increases continuously with the Co content, from 2.35 μ_B in the Co-free area up to 2.76 μ_B in the Co richest area (50% Co). The absolute value reaches the higher range of reported values for $L1_0$-FePt, or Fe_3Pt **[23]**. However, the large dispersion of the absolute values found in the literature show its high sensitivity to the chemical and structural order **[23,26]**. The proximity of Fe to Co atoms favors the increase of the Fe atomic moment, as predicted by the rigid band model of Slater-Pauling, and empirically shown on B2-FeCo **[29]**.

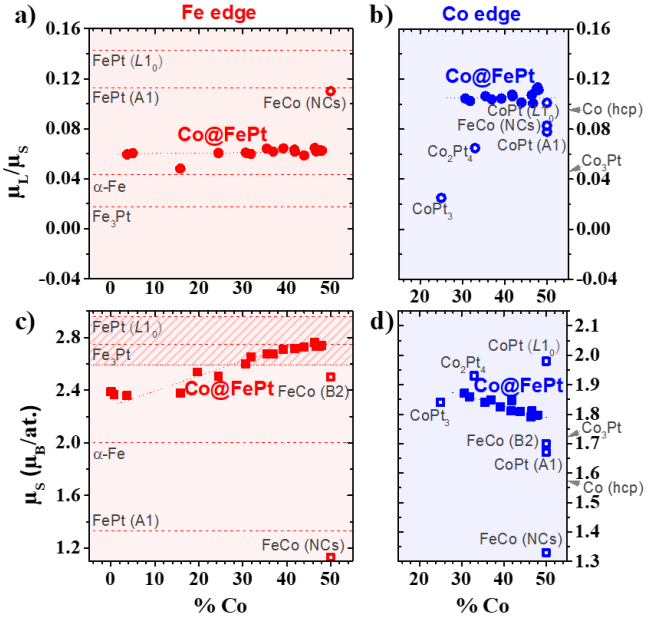

Fig. 4. Orbital/spin moment ratio for Fe (a) and Co (b), and effective spin moment for Fe (c) and Co (d), as a function of Co content. Our results (solid symbols) are compared to some references (open symbols) for bulk and nanoclusters (NCs) (from **[27, 28, 30–33]**).

μ_S(Fe) increases linearly, with a slight change of slope at around 35% Co. In the Fe-Pt alloy, the structural transition from tetragonal $L1_0$ to fcc $L1_2$ is expected to occur between 65% and 68% Fe, with potential intermediate A1 solid solution fcc **[30]**. XRD analysis of the Co-Fe-Pt alloyed films showed a phase transition from $L1_0$ to $L1_2$ between 32% and 48% Co (not shown). However, given that the orbital moment of Fe, μ_L(Fe), is greater in the $L1_0$ phase than in the $L1_2$ phase, this structural change would lead to a drastic decrease of μ_L(Fe) when the Co content increases. Instead, here, the μ_L/μ_S ratio remains nearly constant, suggesting a similar trend for both μ_L(Fe) and μ_S(Fe). We already reported an EXAFS study

of the chemical structure of Co@FePt nanocomposite films **[6]**, which showed that Co-rich regions are well described by fcc $(Co,Fe)_3Pt$ chemical environment. This is in line with the present finding that μ_S(Fe) is closer to the values reported for Fe_3Pt at high Co content.

As opposed to μ_S(Fe), μ_S(Co) decreases linearly when the Co content increases, from 1.87 μ_B at low concentration to 1.79 μ_B at high Co content. Interestingly, one can observe that reported values of are larger in CoPt **[23,26,28**] than Co (hcp) **[19]**. This decay of μ_S(Co) is in good agreement with the persistence of Co-rich regions after annealing, and larger Co-rich cores when the Co content increases. The absolute value of μ_S(Co) ranges from 1.98 μ_B in disordered CoPt **[26]** or 1.62 μ_B in bulk hcp Co **[19]**. However, the absolute value of μ_S(Co) in our case must be taken with caution as the number of holes in NPs are often found to differ from the one of the bulk state **[31,32]**. Moreover, Eastham *et al* showed that surface-induced anisotropy in NPs can lead to a lift **[33]** or a reinforcement **[34]** of the orbital moment quenching, depending on the NPs' size and chemical environment.

Contrary to μ_L(Fe), we found that μ_L(Co) remains nearly constant, at 0.21 μ_B, over the whole range of concentration. Like in Fe-Pt alloy, it is established that the proximity effect of Co and Pt on the Co magnetic moment highly depends on the structure. An increase in μ_L(Co) was predicted in tetragonalized Fe-Co alloys **[35]**. In our nanocomposite films, the tetragonal $L1_0$ matrix may induce a partial but limited distortion of the cubic lattice of Co-rich inclusion. The experimental work of Ueno *et al.* on ultra-thin Co layers sandwiched in between Pt layers showed that as the fraction of Co-Pt bonds with respect to Co-Co increases, μ_S(Co) and μ_L(Co) decrease while the ratio μ_L/μ_S is constant **[36]**. Our findings are similar for the dependence of μ_S(Co), not for μ_L(Co). However, one can notice that there is no general agreement in literature. Density functional theory-generalized gradient approximation (DFT-GGA) computations on small CoPt alloyed clusters by Hu *et al.* **[37]** revealed a systematic increase of the Co magnetic moment as the number of Co-Pt bonds increases.

The ratio μ_L/μ_S at both Fe and Co edges does not vary with the overall composition (**Fig.4a,b**), showing a similar variation of μ_S and μ_L for each element. Its absolute value does not depend on the number of holes **[21,22]**, and remains in between the $L1_0$ phase and the $L1_2$ phase for Fe, which could suggest a coexistence of the two structures. As for Co, the ratio μ_L/μ_S is in the high range of reported values in Co-Pt alloy. The high value of μ_L could be of structural origin in the graded interface between the Co-NPs and the matrix.

TABLE I
FE MOMENTS AS A FUNCTION OF THE CO CONTENT

%Co	μ_L (30°)	μ_L (90°)	μ_S (30°)	μ_S (90°)	μ_L/μ_S (30°)	μ_L/μ_S (90°)
0	0.05	0.13	2.52	2.36	0.020	0.055
25	0.12	0.15	2.59	2.51	0.046	0.060
50	0.12	0.17	2.74	2.74	0.044	0.067

TABLE II
CO MOMENTS AS A FUNCTION OF THE CO CONTENT

%Co	μ_L (30°)	μ_L (90°)	μ_S (30°)	μ_S (90°)	μ_L/μ_S (30°)	μ_L/μ_S (90°)
25	0.21	0.19	2.06	1.85	0.10	0.10
50	0.22	0.20	1.90	1.78	0.12	0.11

Samples were probed at two different angles, at 90° (the X-ray beam is perpendicular to the sample plane, and the electric field lies in the plane of the sample) and at 30° (with thus a non-zero out-of-plane component of the electric field) to investigate the magnetocrystalline anisotropy **[38,39]**. The results are summarized in **Table I** for Fe and **Table II** for Co.

At the Fe edges, the out-of-plane μ_L is systematically larger. This is even stronger in the regions that contain Co. At the Co edges, in contrast, the in-plane μ_L is about 10% higher. Note that as-deposited Co-NPs are in a fcc structure and are randomly oriented. Our findings would translate in a film plane that is hard for μ_L(Fe) but easy for μ_L(Co). However, several effects qualify this conclusion about the anisotropy of the orbital moment. Indeed, spin-orbit coupling and interface roughness between hetero-atoms may lead to an in-plane spin reorientation, overshadowing the magnetocrystalline anisotropy. In particular, it has been shown that the presence of intermixing may lead to the orbital anisotropy not being proportional to magnetocrystalline anisotropy **[40,41]**. Besides, it is well known that TEY measurements suffer from saturation effect, which results in a recorded signal not proportional to the cross-section, especially at grazing incidence, and this effect is more pronounced for Fe than for Co atoms **[18]**.

IV. CONCLUSION

To conclude, compositionnally-graded $Co_x@(FePt)_{100-x}$ nanocomposite films (x varying from 0 to 50%) were prepared by co-deposition from two independent MS-LECBD and e-beam evaporation techniques. We used combined local characterization techniques to investigate the dependence of the magnetic properties on the concentration of Co-NP inclusions. Interestingly, for any studied composition, the measured coercivity is greater in the nanocomposite films than in the homogeneous alloyed films, as expected in a two-phase exchange spring magnet. Fe and Co magnetic moments were quantified using XMCD for the first time in such compositionnally-graded $Co_x@(FePt)_{100-x}$ nanocomposite films, which showed significant variations over the studied range of composition. Fe spin and orbital moments are found to increase with the Co content. Oppositely, Co spin and orbital moments decrease. These experimental findings could be of great interest for the design of semi-hard nanocomposite films with a fine tune of magnetization reversal.

ACKNOWLEDGMENT

This work is supported by the ANR through the project SHAMAN (ANR-16-CE09-0019), and the doctoral school ED PHAST. The authors thanks Rémy Fulcrand and Agnès Piednoir (ILM laboratory) for fruitful discussion and technical support in the cleanroom and AFM experiments. XAS and XMCD experiments were conducted on the DEIMOS

beamline at SOLEIL Synchrotron, France. We are grateful to the SOLEIL staff for smoothly running the facility.

REFERENCES

[1] M. H. Kryder, E. C. Gage, T. W. McDaniel, W. A. Challener, R. E. Rottmayer, G. Ju, Y.-T. Hsia, and M. F. Erden, Heat assisted magnetic recording, Proceedings of the IEEE 96, 1810 (2008).

[2] K. Hono, Y.K. Takahashi, $L1_0$ FePt Granular films for heat-assisted magnetic recording media. In ultrahigh density magnetic recording; G. Varvaro, F. Casoli, Eds.; Pan Stanford Publishing: Singapore, 2016; pp. 246–277.

[3] D. Wen, F. Bai, Y. Wang, Z. Zhong, and H. Zhang, Tailoring of the soft magnetic property and uniaxial anisotropy of magnetostrictive films by interlayer, Journal of Applied Physics 113, 17A309 (2013).

[4] T. Seki, T. Shima, and K. Takanashi, Fabrication of in-plane magnetized FePt sputtered films with large uniaxial anisotropy, Journal of magnetism and magnetic materials 272, 2182 (2004).

[5] H. Zeng, S. Sun, J. Li, Z. Wang, and J. Liu, Tailoring magnetic properties of core/shell nanoparticles, Applied Physics Letters 85, 792 (2004).

[6] C. Paleo, V. Dupuis, F. Wilhelm, A. Rogalev, O. Proux, O. Boisron, I. Kieffer, T. Epicier, M. Bugnet, and D. Le Roy, Interplay between local structure and magnetic properties of graded exchange-coupled Co@FePt nanocomposite films, Physical Review B, 7 (2020).

[7] M. L. Green, I. Takeuchi, and J. R. Hattrick Simpers, Applications of high throughput (combinatorial) methodologies to electronic, magnetic, optical, and energy-related materials, Journal of Applied Physics 113, 9 1 (2013).

[8] A. J. Zambano, H. Oguchi, I. Takeuchi, Y. Choi, J. S.Jiang, J. P. Liu, S. E. Lofland, D. Josell, and L. A. Bendersky, Dependence of exchange coupling interaction on micromagnetic constants in hard/soft magnetic bilayer systems, Physical Review B 75, 144429 (2007).

[9] A. Finkler, D. Vasyukov, Y. Segev, L. Neeman, Y. Anahory, Y. Myasoedov, M. Rappaport, M. Huber, J. Martin, A. Yacoby, et al., Nano-sized squid-on-tip for scanning probe microscopy, in Journal of Physics: Conference Series, Vol. 400 (IOP Publishing, 2012) p. 052004.

[10] Y. Shperber, N. Vardi, E. Persky, S. Wissberg, M. E. Huber, and B. Kalisky, Scanning squid microscopy in a cryogen-free cooler, Review of Scientific Instruments 90, 053702 (2019).

[11] D. Le Roy, G. Shaw, R. Haettel, K. Hasselbach, F. Dumas-Bouchiat, D. Givord, and N. M. Dempsey, Fabrication and characterization of polymer membranes with integrated arrays of high performance micro-magnets, Materials Today Communications 6, 50 (2016).

[12] A. Oral, S. Bending, and M. Henini, Real-time scanning hall probe microscopy, Applied physics letters 69, 1324418 (1996).

[13] A. Dias, G. Gomez, D. Givord, M. Bonfim, and N. M. Dempsey, Preparation and characterisation of compositionally graded SmCo films, AIP Advances 7, 056227422 (2017).

[14] V. Dupuis, G. Khadra, A. Hillion, A. Tamion, J. Tuaillon-Combes, L. Bardotti, and F. Tournus, Intrinsic magnetic properties of bimetallic nanoparticles elaborated by cluster beam deposition, Physical Chemistry Chemical Physics 17, 27996–28004 (2015).

[15] M. Jamet, W. Wernsdorfer, C. Thirion, D. Mailly, V. Dupuis, P. Melinon, and A. Perez, Magnetic anisotropy of a single cobalt nanocluster, Physical Review Letters 86, 4676–4679 (2001).

[16] H. Zeng, M. L. Yan, N. Powers, and D. J. Sellmyer, Orientation-controlled nonepitaxial l10 CoPt and FePt films, Applied Physics Letters 80, 2350–2352 (2002).

[17] P. Ohresser, E. Otero, F. Choueikani, K. Chen, S. Stanescu, F. Deschamps, T. Moreno, F. Polack, B. Lagarde, F. Marteau, and et al., Deimos: A beamline dedicated to dichroism measurements in the 350–2500 eV energy range, Rev. Sci. Instrum. , 9 (2014).

[18] R. Nakajima, J. Stohr, and Y. U. Idzerda, Electron yield saturation effects in L-edge X-ray magnetic circular dichroism spectra of Fe, Co, and Ni, Physical Review B 59, 6421–6429 (1999).

[19] C. T. Chen, Y. U. Idzerda, H.-J. Lin, N. V. Smith, G. Meigs, E. Chaban, G. H. Ho, E. Pellegrin, and F. Sette, Experimental confirmation of the X-ray magnetic circular dichroism sum rules for iron and cobalt, Physical Review Letters 75, 152–155 (1995).

[20] J. M. D. Coey, Magnetism and Magnetic Materials, 1st ed. (Cambridge University Press, 2001).

[21] B. T. Thole, P. Carra, F. Sette, and G. van der Laan, X-ray circular dichroism as a probe of orbital magnetization, Physical Review Letters 68, 1943–1946 (1992).

[22] P. Carra, B. T. Thole, M. Altarelli, and X. Wang, X-ray circular dichroism and local magnetic fields, Physical Review Letters 70, 694–697 (1993).

[23] I. Galanakis, M. Alouani, and H. Dreyss´e, Calculated magnetic properties of low-dimensional systems: the AuCu- and AuCu3-type ferromagnets, Journal of Magnetism and Magnetic Materials 242–245, 27–32 (2002).

[24] G. Khadra, Magnetic and structural properties of size-selected FeCo nanoparticle assemblies, Theses, Université Claude Bernard Lyon 1 (2015).

[25] S. Sakamoto, K. Srinivasan, R. Zhang, O. Krupin, K. Ikeda, G. Shibata, Y. Nonaka, Z. Chi, M. Sakamaki, K. Amemiya, and et al., Effects of cobalt substitution in L10-(Fe,Co)Pt thin films, Physical Review B 96, 144437 (2017).

[26] V. Dupuis, G. Khadra, S. Linas, A. Hillion, L. Gragnaniello, A. Tamion, J. Tuaillon-Combes, L. Bardotti, F. Tournus, E. Otero, and et al., Magnetic moments in chemically ordered mass-selected CoPt and FePt clusters, Journal of Magnetism and Magnetic Materials 383, 73–77 (2015).

[27] J. S. Faulkner and R. G. Jordan eds., Metallic Alloys: Experimental and Theoretical Perspectives (Kluwer, Dordrecht, Springer Netherlands, 1994).

[28] O. Sipr, J. Minar, S. Mankovsky, and H. Ebert, Influence of composition, many-body effects, spin-orbit coupling, and disorder on magnetism of Co-Pt solid-state systems, Physical Review B 78, 12 (2008).

[29] J. M. MacLaren, T. C. Schulthess, W. H. Butler, R. Sutton, and M. McHenry, Electronic structure, exchange interactions, and curie temperature of feco, Journal of Applied Physics 85, 4833–4835 (1999).

[30] C. J. Smithells, W. F. Gale, and T. C. Totemeier, Smithells metals reference book, 8th ed. (Elsevier Butterworth-Heinemann, 2004).

[31] H. Basch, M. D. Newton, and J. W. Moskowitz, The electronic structure of small nickel atom clusters, The Journal of Chemical Physics 73, 4492–4510 (1980).

[32] F. Luis, F. Bartolome, F. Petroff, J. Bartolome, L. M. Garcıa, C. Deranlot, H. Jaffres, M. J. Martınez, P. Bencok, F. Wilhelm, and et al., Tuning the magnetic anisotropy of Co nanoparticles by metal capping, Europhysics Letters (EPL) 76, 142–148 (2006).

[33] D. A. Eastham, P. M. Denby, A. Harrison, I. W. Kirkman, and A. G. Whittaker, Enhanced magnetocrystalline anisotropy in deposited cobalt clusters, Journal of Physics: Condensed Matter 14, 605–612 (2002).

[34] D. A. Eastham, Y. Qiang, T. H. Maddock, J. Kraft, J.-P. Schille, G. S. Thompson, and H. Haberland, Quenching of ferromagnetism in cobalt clusters embedded in copper, Journal of Physics: Condensed Matter 9, L497–L502 (1997).

[35] T. Burkert, L. Nordstrom, O. Eriksson, and O. Heinonen, Giant magnetic anisotropy in tetragonal FeCo alloys, Physical Review Letters 93, 027203 (2004).

[36] T. Ueno, J. Sinha, N. Inami, Y. Takeichi, S. Mitani, K. Ono, and M. Hayashi, Enhanced orbital magnetic moments in magnetic heterostructures with interface perpendicular magnetic anisotropy, Scientific Reports 5, 14858 (2015).

[37] W. Hu, H. Yuan, H. Chen, G. Wang, and G. Zhang, Structural and magnetic properties of CoPt clusters, Physics Letters A 378, 198 (2014).

[38] P. Bruno, Tight-binding approach to the orbital magnetic moment and magnetocrystalline anisotropy of transition-metal monolayers, Physical Review B 39, 865–868 (1989).

[39] J. Stohr, Exploring the microscopic origin of magnetic anisotropies with X-ray magnetic circular dichroism (XMCD) spectroscopy, Journal of Magnetism and Magnetic Materials 200, 470–497 (1999).

[40] P. Bruno and J. P. Renard, Magnetic surface anisotropy of transition metal ultrathin films, Applied Physics A Solids and Surfaces 49, 499–506 (1989).

[41] C. Andersson, B. Sanyal, O. Eriksson, L. Nordstrom, O. Karis, D. Arvanitis, T. Konishi, E. Holub-Krappe, and J. H. Dunn, Influence of ligand states on the relationship between orbital moment and

magnetocrystalline anisotropy, Physical Review Letters 99, 177207 (2007).